# Surfactant-Free Aqueous Dispersions of Shape- and Size-Controlled Zirconia Colloidal Nanocrystal Clusters with Enhanced Photocatalytic Activity

Yi Xia,[†,‡] Qian Sun,[*,†] Dan Wang,[†] Xiao-Fei Zeng,[‡] Jie-Xin Wang,[*,†,‡] and Jian-Feng Chen[†,‡]

[†]Beijing Advanced Innovation Center for Soft Matter Science and Engineering, State Key Laboratory of Organic-Inorganic Composites, and [‡]Research Center of the Ministry of Education for High Gravity Engineering and Technology, Beijing University of Chemical Technology, Beijing 100029, PR China

S *Supporting Information*
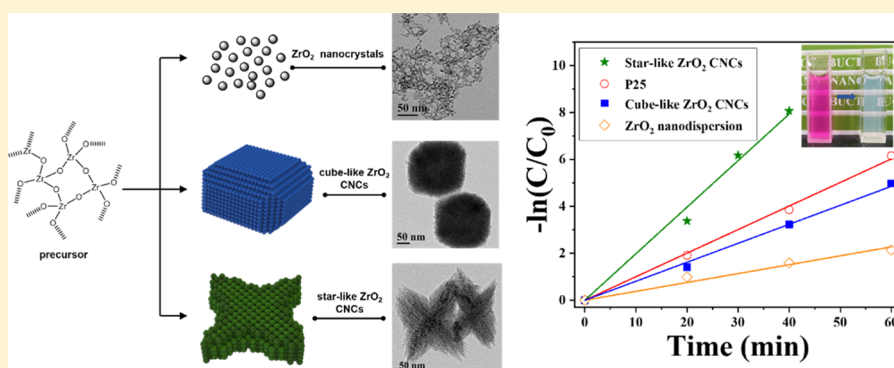
ABSTRACT: Colloidal nanocrystal clusters (CNCs) are formed by clustering nanocrystals into secondary structures, which represent a new class of materials and have attracted considerable attention, owing to their unique collective properties and novel functionalities achieved from the ensembles in addition to the properties of each individual subunit. Here, we design a simple route to prepare aqueous dispersions of highly stable ZrO_2 CNCs with tunable shape and size without modification. ZrO_2 CNCs are composed of many ZrO_2 nanocrystals each with a size of about 7 nm and possess a mesoporous structure. Both cube-like and star-like shapes of CNCs can be achieved by using different alkaline sources, while the size of CNCs can be adjusted by changing the hydrothermal time. The as-prepared aqueous dispersions of ZrO_2 CNCs display an enhanced photocatalytic activity in the degradation of rhodamine B (RhB), compared with ZrO_2 nanodispersions. More interestingly, star-like ZrO_2 CNCs show better photocatalytic degradation properties than those of cube-like counterparts and even commercial P25. Furthermore, ZrO_2 CNCs are easily recycled and can be used for the degradation of a range of dye systems.

INTRODUCTION

In the past two decades, the preparation of colloidal nanoparticles with tunable size and shape is of increasing interest for their novel properties, which cannot be obtained using bulk materials.[1−4] However, recent research appears to be directed toward the controlled clustering of nanoparticle subunits into defined geometric arrangements. Clustering nanoparticles into secondary structures to form so-called colloidal nanoparticle clusters (CNCs) not only combines the size-dependent properties of individual nanoparticles but also makes use of the interactions between nanoparticle building blocks, generating collective properties, and novel functionalities absent in the initial nanoparticles.[5−8] Usually, the preparation strategy of CNCs can be divided into two categories: (i) a one-step route which refers to the synthesis of nanoparticles and their oriented attachment into CNCs in a single step;[9,10] and (ii) a two-step route which means the pre-preparation of nanoparticles as building kits and the subsequent clustering into CNCs via some methods, such as

solvent evaporation, electrostatic attraction, spray drying,[11] or interfacial tension.[12−17] Although the two-step route has the advantage of being more flexible and universal for generating highly configurable structures, the one-step route is more efficient and quicker.

Metal oxides such as TiO_2,[18−20] ZnO,[21−23] Fe_2O_3,[24−26] Bi_2O_3,[27,28] ZrO_2,[29−32] CuO,[33,34] NiO,[35,36] and CeO_2[37,38] have been intensively explored as effective photocatalysts to degrade various organic and inorganic pollutants in wastewater. In particular, nanosized metal oxide photocatalysts exhibit good degradation properties owing to their well-known nanoeffects. Among them, TiO_2 and ZnO nanoparticles attract the most interest. However, there are still several challenges and practical requirements for the development of high-performance photocatalysts for treating wastewater. First, it is desired

for photocatalysts to achieve chemical stability in complicated wastewater surroundings such as variable pH. Second, the stable dispersion of particles in wastewater is necessary to allow enhanced contact between pollutant molecules and photocatalysts, even without agitation or strong turbulence. Third, the construction of hierarchical structures of photocatalysts usually displayed enhanced degradation compared with individual nanoparticles.[33,39−41]

Among various metal oxide photocatalysts, ZrO_2 has proven to be a promising candidate because of its biological and chemical inertness: it can resist both strong acid and alkali, and displays long-term stability against photo and chemical corrosion.[42] Many synthetic approaches have been adopted to prepare various kinds of ZrO_2 nanostructures including sol−gel,[43] precipitation,[31] hydrothermal,[44] and solvothermal methods.[45−49] When ZrO_2 is applied to the degradation of pollutants, ZrO_2 particles with hierarchical structures or special morphologies usually possess better photocatalytic properties than ZrO_2 nanoparticles alone.[30] Thus, ZrO_2 CNCs have potential in photocatalytic degradation applications. Currently, there are only a few reports on the synthesis of ZrO_2 CNCs, which employed a two-step route.[13,15] Furthermore, the preparation of an aqueous dispersion of ZrO_2 CNCs still has a few significant challenges, such as large-scale preparation with controllable shapes, narrow size distributions, and high dispersibility, which we address.

In this work, we present a simple method for the efficient synthesis of an aqueous dispersion of ZrO_2 CNCs with high stability and concentrations, controlled sizes, and shapes without any surface modifications. The synthesis of ZrO_2 CNCs on a 10 g scale has been accomplished without the scale-up effect, which demonstrates the great potential of this route. Continuous size tuning of ZrO_2 CNCs can be achieved from 74 to 170 nm by controlling only the hydrothermal time. Salt ions such as Na^+ and Cl^- have been shown to play an important role in controlling the shape of ZrO_2 CNCs to cube-like or star-like morphologies. The nanoscale ZrO_2 primary subunits with an average size of 7 nm were oriented toward each other, thereby generating mesoporous network structures. In addition, rhodamine B (RhB) was chosen as a probe molecule to evaluate the photocatalytic performances of the ZrO_2 CNCs. Because of the unique collective properties, aqueous dispersions of ZrO_2 CNCs exhibit obviously enhanced photocatalytic activity compared with ZrO_2 nanodispersions. The star-like ZrO_2 CNCs possess better photocatalytic degradation properties than those of cube-like ZrO_2 CNCs and even commercial P25.

■ EXPERIMENTAL SECTION

Chemicals. Zirconium oxychloride octahydrate ($ZrOCl_2·8H_2O$) and sodium hydroxide (NaOH) were purchased from Beijing Chemical Reagent Co. Tetramethylammonium hydroxide aqueous solution ($N(CH_3)_4OH$, 10 wt %), commercial TiO_2 (P25), RhB, methyl violet, and Congo red were purchased from Aladdin Bio-Chem Technology Co. All the chemical reagents were analytically pure and used without further purification. Deionized water was purified by a water purification system (RO-DI plus, Hitech, PRC).

Preparation of Aqueous Dispersions of Cube-like and Star-like ZrO_2 CNCs. In a typical procedure for production of an aqueous dispersion of cube-like ZrO_2 CNCs, 32.225 g of $ZrOCl_2·8H_2O$ and was dissolved in 500 mL of deionized water at 25 °C under vigorous stirring. Afterward, 4.90 mL of $N(CH_3)_4OH$ aqueous solution (10 wt %) was added dropwise (two drops per 1 s). Then, the mixture was stirred at 70 °C for 3 h, the as-obtained zirconium hydroxide

precursor was loaded into a Teflon-lined, stainless steel autoclave and heat treated. After cooling to room temperature, the products were collected and washed by centrifugation with deionized water three times to form an aqueous dispersion of cube-like ZrO_2 CNCs.

Star-like ZrO_2 CNCs were obtained by replacing $N(CH_3)_4OH$ with NaOH. $ZrOCl_2·8H_2O$ (32.225 g) was dissolved in 400 mL of deionized water at 25 °C under vigorous stirring. NaOH (4.0 g) was dissolved in 100 mL deionized water, and added dropwise into the above $ZrOCl_2$ aqueous solution (one drop per 5 s). Then the mixture was stirred at 70 °C for 3 h, the as-obtained zirconium hydroxide precursor was hydrothermally treated, and washed by centrifugation with deionized water three times, obtaining an aqueous dispersion of star-like ZrO_2 CNCs.

Photocatalytic Activity Test. The photocatalytic activity test of aqueous dispersions of ZrO_2 CNCs was performed without agitation for the degradation of RhB under UV irradiation at room temperature. Typically, 100 μL of aqueous dispersion of ZrO_2 CNCs (100 g/L) and 100 μL of RhB aqueous solution (1 g/L) were added to 100 mL of deionized water in a 100 mL bottle, forming into an aqueous solution of RhB (10 ppm). A 300 W high-pressure mercury lamp (λ = 365 nm) was positioned inside a cylindrical vessel and surrounded by a circulating water jacket for cooling. Prior to the photocatalytic reaction, the RhB aqueous solution was placed in darkness for 30 min to ensure equilibrium between dye molecules and ZrO_2 CNCs. Afterward, the above RhB aqueous solution was irradiated with UV light from a high-pressure mercury lamp. A mixture sample (5.0 mL) was periodically withdrawn at time intervals of 20 min during a total irradiation time of 160 min, and centrifuged at 12 000 rpm for 5 min to separate the photocatalyst particles from the solution. The filtrate sample was analyzed to determine the concentration of RhB by absorbance measurement using a UV−vis spectrometer at the maximum absorption wavelength of RhB, which is 554 nm.[18]

For comparison of photocatalytic activity, an aqueous dispersion of primary ZrO_2 nanocrystals with an average size of 7 nm was also prepared with almost the above same two procedures, in which all the salt ions were removed via dialysis before the hydrothermal treatment, and no agitation was needed in the photocatalytic test. In addition, commercial P25 powders were also used. The photocatalytic test was performed under stirring to ensure the dispersion of P25 nanoparticles in water. Other dyes such as methyl violet and Congo red were also adopted to examine the photocatalytic activity of ZrO_2 CNCs.

Characterization. The size and morphology of ZrO_2 CNCs were examined with a scanning electron microscope (SEM) (JSM-6701F, JEOL, Japan) and a transmission electron microscope (TEM) (JEM-2100, JEOL, Japan). The surface potential of ZrO_2 CNCs was measured with zeta potential analyzer (Nano-ZS90, Malvern, Britain). The crystalline structure of the ZrO_2 sample was examined with an X-ray diffractometer (XRD-6000, Shimadzu, Japan) equipped with Cu Kα radiation, an accelerating voltage of 40 kV, and a current of 40 mA. The scanning range was 10° to 80° and the scanning rate was 5°/min with a step size of 0.02°. X-ray photoelectron spectroscopy (XPS) was performed using an ESCALAB 250 XPS System with a monochromated Al Kα (150 W) source. The Fourier transform infrared (FTIR) spectrum was recorded with a Nicolet 6700 spectrometer (Nicolet Instrument Co., USA) in the range of 400−4000 cm^{-1}. The nitrogen adsorption−desorption isotherm was measured on ASAP (2010, USA), in which the sample was first outgassed in vacuum at 473 K overnight and the measurement was then carried out at 77 K. The pore size distribution (PSD) was determined by the Barret−Joyner−Halenda (BJH) method and the surface area was calculated by the Brunauer−Emmett−Teller (BET) method. The ultraviolet−visible diffuse reflectance spectrum (UV−DRS) of the sample was recorded by using an ultraviolet−visible infrared spectrophotometer (lambda 750) manufactured by Perki-nElmer Instrument Co. Electrochemical and photoelectrochemical measurements were performed in three-electrode quartz cells (the counter electrode: platinum wire; the reference electrodes: saturated calomel electrodes; the working electrode: ITO) with a 0.5 M Na_2SO_4

electrolyte solution under irradiation of 300 W high-pressure mercury lamp (λ = 365 nm), which was the same with the light in photocatalytic activity tests.

RESULTS AND DISCUSSION

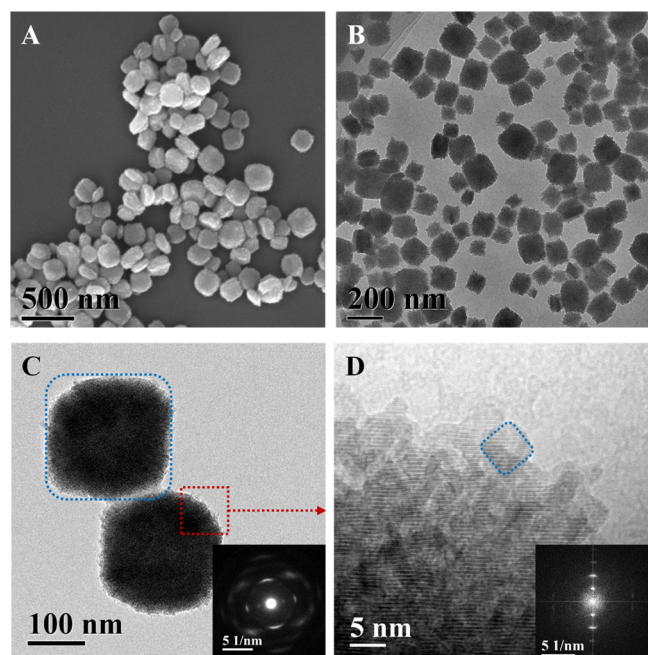Figure 1 shows the representative SEM, TEM, HRTEM images, and the corresponding selected area electron

Figure 1. SEM (A), TEM (B), HRTEM images (C,D) and the corresponding SAED patterns of the cube-like ZrO_2 CNCs obtained from a hydrothermal temperature of 200 °C for 10 h.

diffraction (SAED) patterns of the cube-like ZrO_2 CNCs obtained at a hydrothermal temperature of 200 °C for 10 h. The as-prepared particles consisted of small primary nanoparticles. They appear to be cubic, with a size length of ca. 170 nm, a plate thickness of ca. 80 nm, and a rough surface (Figure 1A,B). The HRTEM image (Figure 1D) of an edge of one single cluster in Figure 1C (marked by the red rectangle) provides a further vision into the structural information on the clusters. Although ZrO_2 CNCs are polycrystalline materials, the continuous parallel lattice fringes indicate that the stacks of ZrO_2 nanocrystals with a diameter of ca. 7 nm grow in an oriented direction instead of anisotropic growth. For this reason, the SAED pattern of a single ZrO_2 cluster (the inset picture in Figure 1D) reveals a nearly single-crystal-like feature instead of a diffraction ring, which has been reported in the literature.[9,50−52] Different from the single crystalline feature of the selected nanocrystal in Figure 1D, the widened diffraction spots (the inset picture in Figure 1C) indicate slight misalignments among the primary nanocrystals in single CNC.

Figure 2 displays the TEM image of ZrO_2 nanocrystals, SEM images of cube-like ZrO_2 CNCs prepared at a temperature of 200 °C for different hydrothermal times, and the corresponding particle size distributions. As shown in Figure 2A, the transparent aqueous dispersion of ZrO_2 nanocrystals with an average size of 7 nm was obtained when all salt ions were removed before the hydrothermal treatment. However, when Cl$^-$ were not present for the hydrothermal treatment, ZrO_2 nanocrystals were aggregated with preferred orientation to
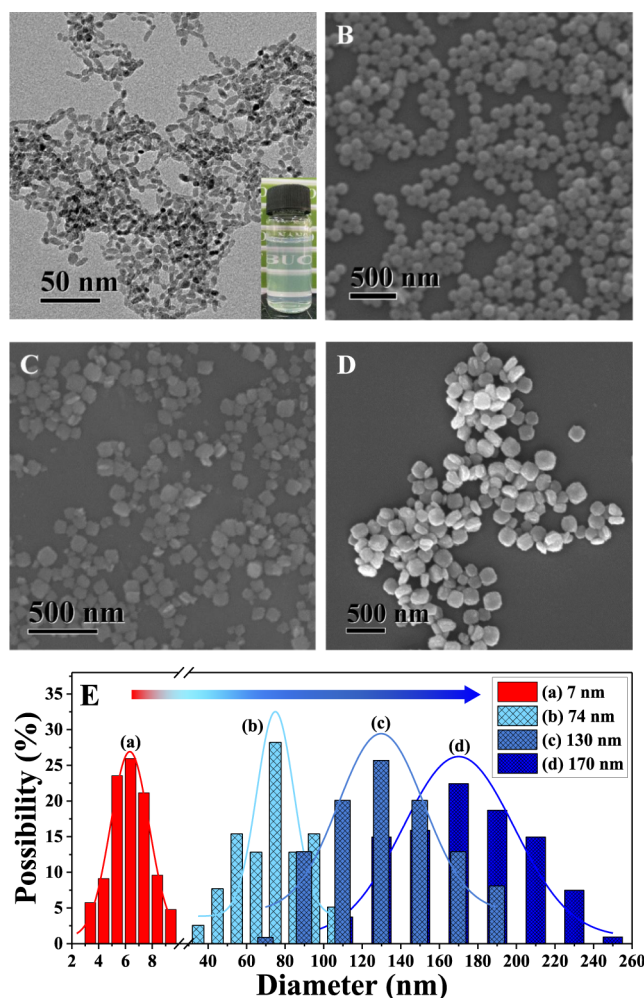

Figure 2. TEM image of ZrO_2 nanocrystals (A); SEM images of cube-like ZrO_2 CNCs prepared at a hydrothermal temperature of 200 °C for 6 h (B), 8 h (C), 10 h (D); and the corresponding particle size distributions (E) (for each histogram, over 100 particles were measured).

cube-like ZrO_2 CNCs by a self-assembly of ZrO_2 nanocrystals. $N(CH_3)_4OH$ was proved to merely be a hydrolytic accelerating agent instead of a shape controller because ZrO_2 CNCs retained a very similar morphology by replacing $N(CH_3)_4OH$ with ammonia hydroxide (Figure S1). The above results indicate that the presence of Cl$^-$ during the hydrothermal process plays a key role in the formation of cube-like ZrO_2 CNCs. Furthermore, it can be found that the average size of ZrO_2 CNCs increased from 74 to 170 nm, while the particle size distribution also became wider with the prolonged hydrothermal time from 6 to 10 h. However, hydrothermal temperature (150−240 °C) has little effect on the average size and the shape of ZrO_2 CNCs, as shown in Table 1 and TEM images of Figure S2. The possible reason of this interesting

Table 1. Experimental Parameters for the Preparation of Typical Cube-like ZrO_2 CNCs

hydrothermal temperature (°C)	time (h)	size (nm)
150−180−200−220−240	6	ca. 74
150−180−200−220−240	8	ca. 130
150−180−200−220−240	10	ca. 170

C

observation is that the clustering of ZrO_2 nanocrystals in this case mainly depends on hydrothermal time, and the ZrO_2 nanocrystal clustering is a slow self-assembly process only occurring at a relatively high temperature (>150 °C) for the formation of ZrO_2. The lower temperature (such as 130 °C) has a very low yield of 10%.

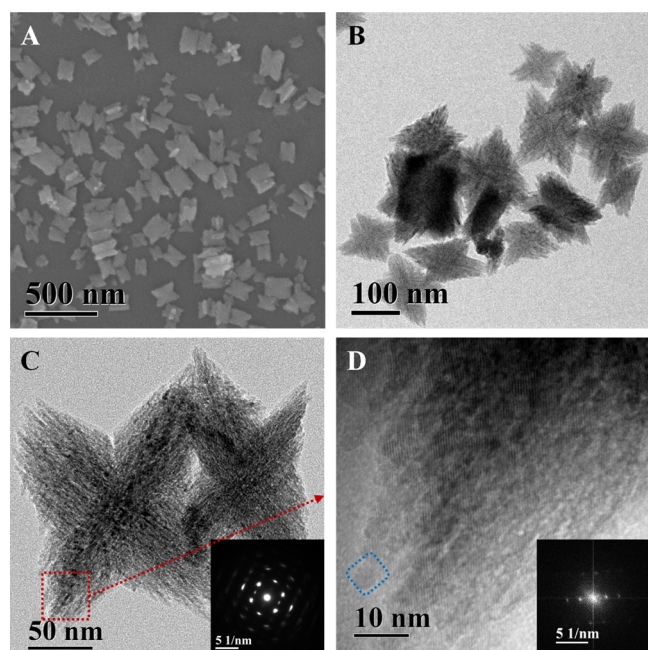Figure 3 shows the representative SEM, TEM, HRTEM images, and the corresponding SAED patterns of star-like ZrO_2

Figure 3. SEM (A), TEM (B) and HRTEM images (C,D) and the corresponding SAED patterns of star-like ZrO_2 CNCs prepared using a hydrothermal temperature of 200 °C for 10 h.

CNCs prepared at a hydrothermal temperature of 200 °C for 10 h. In this case, the alkali source of $N(CH_3)_4OH$ was replaced with NaOH. The morphology of ZrO_2 CNCs was significantly changed from cube-like to star-like, possibly ascribed to the combined action of Cl^- and Na^+ for achieving shape tuning. Several lines of evidence point to salt ions as the dominant control during particle−particle aggregation,[5,9,53] when oriented attachment occurs in aqueous or water-miscible systems. The schematic formation process is shown in Scheme 1. Similarly, the continuous and clear lattice fringe, and nearly single-crystal-like SAED pattern indicate the high crystallinity and oriented aggregation of nanocrystals with a size of about 7 nm, forming the star-like ZrO_2 CNCs. XRD characterizations of the as-prepared cube-like, star-like ZrO_2 CNCs, and ZrO_2 nanocrystals were performed, as shown in Figure S3. The diffraction peaks of three samples were all well indexed to the pure monoclinic phase [space group: $P21/c$ (14)] of ZrO_2 (PDF no. 80-0966). The corresponding XPS spectra in Figure S4 show that Zr $3d_{5/2}$ is located at 182.1 eV and Zr $3d_{3/2}$ is located at 184.4 eV. These results confirm the presence of Zr^{4+} and also demonstrate no chemical shift on ZrO_2 CNCs and nanocrystals.

Figure 4 shows the digital photographs of aqueous dispersions of ZrO_2 CNCs with different solid contents. Despite no surface modification, ZrO_2 CNCs can be stably dispersed in water without precipitation for weeks, mainly attributed to a high surface potential (+37.5 mV). When the

Scheme 1. Proposed Formation Mechanism of ZrO_2 Nanoparticles, Cube-like and Star-like ZrO_2 CNCs
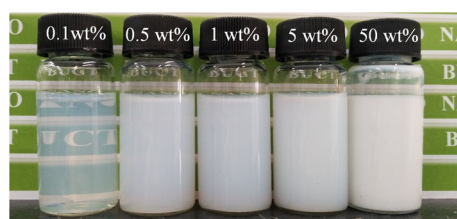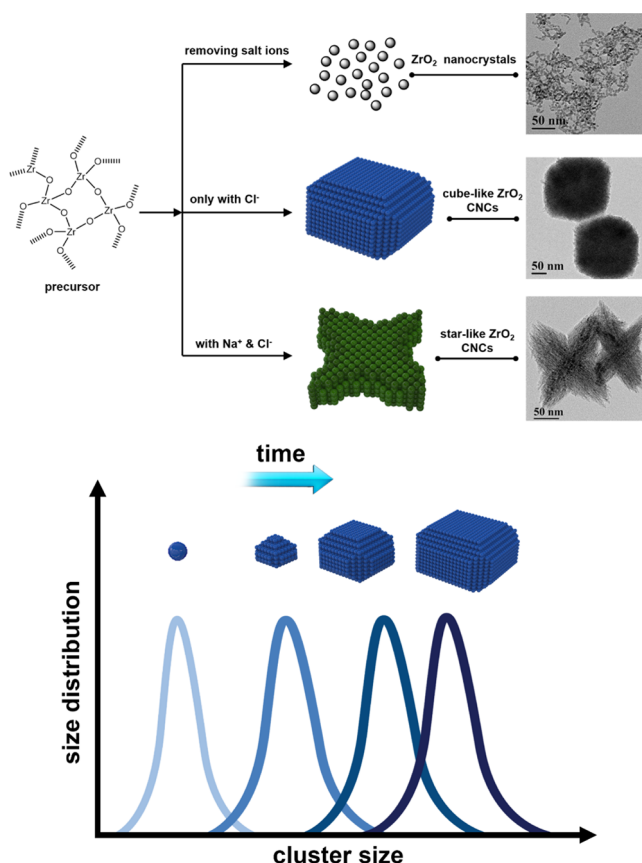

Figure 4. Digital photographs of ZrO_2 CNC dispersions with different solid contents.

solid content was 0.1 wt % (about 1 g/L), the dispersion of ZrO_2 CNCs was clear and transparent, visually identical to water. With increasing ZrO_2 solid content from 0.5 to 50 wt %, the dispersion of ZrO_2 CNCs changed from translucent to milky white. However, ZrO_2 CNCs still kept a high-dispersion stability even at a superhigh solid content of 50 wt %. Furthermore, no use of surface modifiers was required which was helpful to the photocatalytic activity of CNCs. FTIR spectra of two kinds of shaped ZrO_2 CNCs and ZrO_2 nanocrystals also prove the pure ZrO_2 nature (Figure S4).

Figure 5 shows the nitrogen adsorption−desorption isotherms and the corresponding PSDs of cube-like and star-like ZrO_2 CNCs. They were all typical type IV isotherms with a hysteresis loop of type H2, which was associated with capillary condensation taking place in well-developed meso-pores and the limiting uptake over a range of high P/P_0 around 0.7−0.9.[54] The corresponding BJH curves show that both of the two samples have a wide PSD with the concentrated size of ca. 12.4 nm. The BET-specific surface areas were calculated to
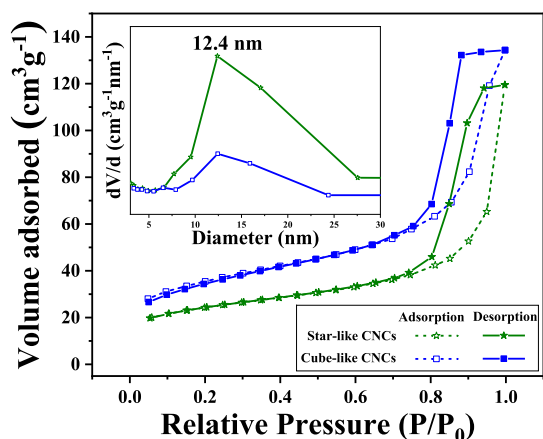
Figure 5. Nitrogen adsorption−desorption isotherms and the PSDs (the inner image) of the cube-like and star-like ZrO_2 clusters, hydrothermally treated at 200 °C for 6 h.

be 120 m^2/g for cube-like, and 81 m^2/g for star-like ZrO_2 CNCs, respectively. This mesoporous framework of hierarchical internanocrystallite and intercluster pores may endow ZrO_2 CNCs high photocatalytic activity because it allows the target molecules to be more accessible to the surfaces of ZrO_2 CNCs.

Figure 6 presents the degradation curves of RhB over cube-like ZrO_2 CNCs prepared at (A) different hydrothermal

temperatures and a fixed hydrothermal time of 6 h, and (B) at a fixed hydrothermal temperature of 200 °C and different hydrothermal times. Although it has almost no effect on the particle size of ZrO_2 CNCs, hydrothermal temperature obviously influences the photocatalytic activity of ZrO_2 CNCs. As shown in Figure 6A, ZrO_2 CNCs prepared at a lower hydrothermal temperature (150 °C) have a much slower degradation rate than those of products obtained at higher temperatures. The products prepared in the range of 200−240 °C have a similar photocatalytic activity, which was higher than that of the counterpart at 180 °C. Thus, the relatively lower hydrothermal temperature of 200 °C was selected in the following study. As shown in Figure 6B, the photocatalytic rate of cube-like ZrO_2 CNCs for RhB significantly improved with the decrease of hydrothermal time from 10 to 6 h. For 6 h product, the degradation of RhB reached 75% in 20 min, and 100% in 60 min. Correspondingly, 8 and 10 h products degraded 100% RhB only in 100 and 140 min. This can be ascribed to the smaller and more uniform particle size of ZrO_2 CNCs, as seen in Figure 2. Therefore, the optimum time is selected to be 6 h.

It is well-known that the clean surface of catalyst particles is crucial to their catalytic properties. Our ZrO_2 CNCs without any modification exhibit much better degradation ability than ZrO_2 CNCs modified by PVP owing to the more exposed activity sites (Figures S5 and S6). Compared with ZrO_2 CNCs@PVP, the complete degradation time of RhB over ZrO_2 was decreased from 160 to 60 min. This means, if possible, the use of organic modifiers should be avoided in the preparation of photocatalysts.

To understand the photocatalytic activity of ZrO_2 CNCs better, P25 (commercially available nanosized TiO_2) and aqueous dispersions of ZrO_2 nanocrystals with no surface modification, and a size very close to nanocrystal subunits of CNCs (ZrO_2 nanodispersions) were selected as references. Figure 7 compares the degradation curves and the corresponding reaction kinetic curves of RhB over aqueous dispersions of cube-like ZrO_2 CNCs, star-like ZrO_2 CNCs, ZrO_2 nano-dispersions, and P25. As we can see from Figure 7A, compared with ZrO_2 nanodispersions, aqueous dispersions of ZrO_2 CNCs display significantly enhanced photocatalytic activity in the degradation of RhB. More interestingly, star-like ZrO_2 CNCs possess better photocatalytic degradation properties than those of the cube-like counterpart and even P25. After 20 min, 96% of RhB can be degraded by star-like ZrO_2 CNCs, and 85% for P25, 74% for cube-like ZrO_2 CNCs, while only 63% for ZrO_2 nanodispersions. The complete degradation times of RhB are 40 min for star-like ZrO_2 CNCs and 60 min for P25 and cube-like ZrO_2 CNCs. Furthermore, the photocatalytic degradation data are fitted by the following Langmuir−Hinshelwood kinetics model equation.

$$\ln(C/C_0) = k_\alpha \times t \tag{1}$$

where k_α is the reaction rate constant (min^{-1}), t is the irradiation time, C_0 is the dye initial concentration and C is the dye concentration at time t. As shown in Figure 7B, a plot of $\ln(C/C_0)$ versus irradiation time shows a good linear relationship, belonging to a pseudo-first-order reaction. In addition, it is noted that oxygen-deficient ZrO_2 with a decreased band gap shows better photocatalytic performances for photochemical catalysis.[42] In this study, the energy band gap of ZrO_2 CNCs (in the range of 5.0−5.85 eV, which is wider than that of TiO_2 (3.2 eV)[55]), did not change, as shown
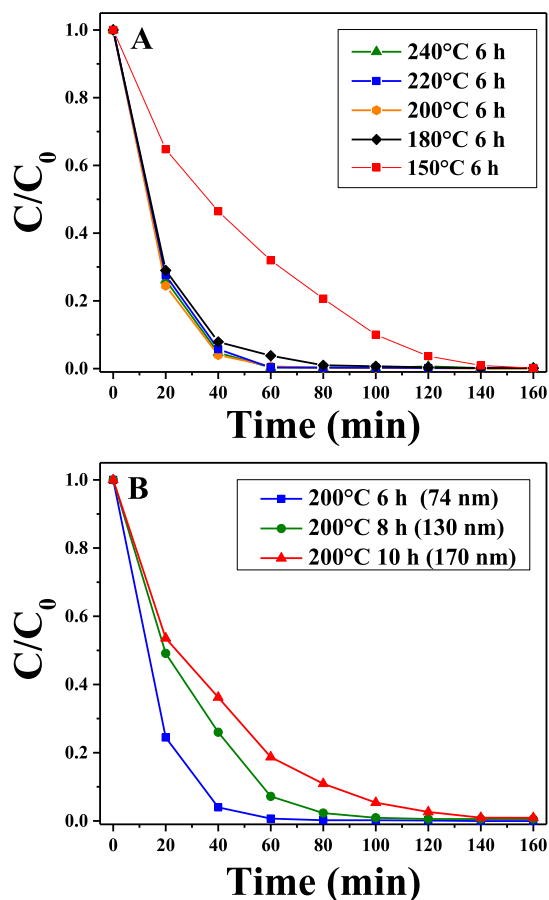

Figure 6. Degradation of RhB over cube-like ZrO_2 CNCs prepared at different hydrothermal temperatures of 150, 180, 200, 220 and 240 °C for 6 h (A); and 200 °C for 6, 8, and 10 h (B).

ation with the light switching several times, the changing tendency of photocurrent generated by these samples was consistent with the order of their photocatalytic activities, as shown in Figure 7.

To further explore the recycling properties of this photocatalyst, star-like ZrO$_2$ CNCs were used multiple times for the degradation of RhB, as shown in Figure 8. After five cycles,
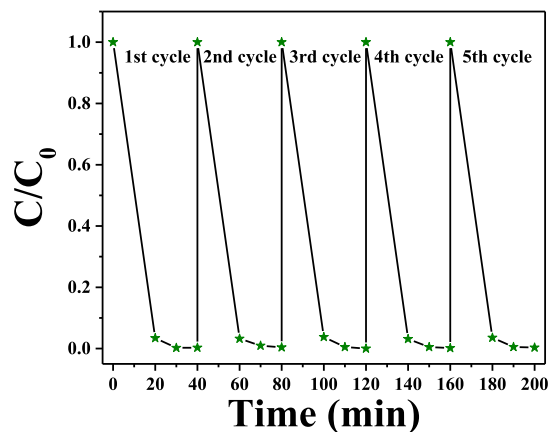
Figure 8. Reusability tests of star-like ZrO$_2$ CNCs prepared at a hydrothermal temperature of 200 °C for 6 h.

there is no decrease of the degradation properties, with the CNCs, exhibiting the same photocatalytic activity. This shows the great potential of ZrO$_2$ CNCs in practical photocatalytic applications. Besides the recycling ability, the feasibility for the degradation of other dyes needs to be explored. Figure 9
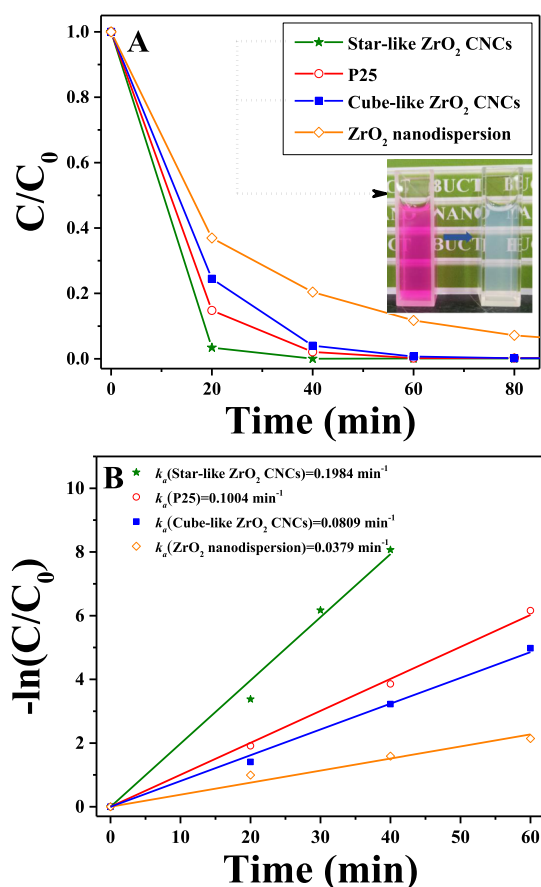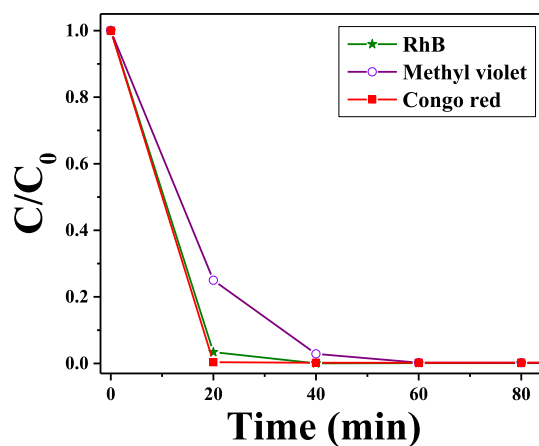

Figure 7. Degradation curves (A) and reaction kinetic curves (B) of RhB over star-like and cube-like ZrO$_2$ CNCs prepared at a hydrothermal temperature of 200 °C for 6 h, aqueous dispersion of ZrO$_2$ nanocrystals and P25.

in Figure S7. However, the degradation rate of RhB over star-like ZrO$_2$ CNCs is calculated to be 0.1984 min^{-1}, which is 1.98 times faster than that of P25. There are two main reasons: one is because of the enhanced collective properties of CNCs. Similar phenomenon are also found in other reported CNCs, such as stronger signals from quantum dot CNCs and much higher saturated magnetization from iron oxide CNCs.[7,10] The second reason is that ZrO$_2$ CNCs have a novel mesoporous structure with a crystalline framework, enabling fast diffusion and adsorption of RhB molecules from solution. In addition, despite the smaller surface area, star-like ZrO$_2$ CNCs have much better photocatalytic activity than cube-like ZrO$_2$ CNCs. This result indicates that the morphology should be a more important factor in determining the photocatalytic activity of the prepared ZrO$_2$ CNCs. A star-like shape with more open structures is more beneficial to the complete contact between dye molecules and ZrO$_2$ nanoparticles than cube-like shape with a relatively closed structure.

The photocurrent measurement was used to reflect the separation of the photogenerated electron−hole pair in the photocatalyst, and the rate is positively relevant to the photocatalytic activity of the material.[56] Figure S8 shows the photocurrent density−time curves of star-like ZrO$_2$ CNCs, cube-like ZrO$_2$ CNCs, aqueous dispersion of ZrO$_2$ nanocrystals, and P25 samples generated in the electrolyte under UV light. When the light was on, the photocurrent of samples was generated immediately. Although there was intensity attenu-

Figure 9. Degradation curves of different dyes over star-like ZrO$_2$ CNCs prepared at a hydrothermal temperature of 200 °C for 6 h.

presents the degradation curves of different dyes over star-like ZrO$_2$ CNCs. Besides RhB, star-like ZrO$_2$ CNCs also exhibit excellent photocatalytic activities for methyl violet and Congo red.

■ CONCLUSIONS

Highly stable and concentrated aqueous dispersions of ZrO$_2$ CNCs with tunable shape and size can be efficiently prepared via a simple method without any modification. The as-prepared ZrO$_2$ CNCs consist of ZrO$_2$ nanocrystals with a size of about 7 nm, and have a mesoporous structure with an average pore size of 12.4 nm. Cube-like and star-like shapes of

CNCs can be tuned by using different alkaline sources, and the particle size can be adjusted by changing the hydrothermal time. The studies on the photocatalytic activity of ZrO_2 CNCs for the photodegradation of RhB under UV irradiation indicate that the ZrO_2 CNCs exhibit much better degradation properties than ZrO_2 nanodispersions owing to the unique enhanced collective properties of CNCs. The degradation rate of RhB over star-like ZrO_2 CNCs is 1.98 times faster than that of commercial P25. More importantly, ZrO_2 CNCs possess good environmental stability, reusability property, and applicability for the degradation of more dye systems. It could be envisioned that such CNCs with excellent photocatalytic performances are possible to be candidates for many advanced photocatalytic applications.

■ ASSOCIATED CONTENT

ⓢ Supporting Information

The Supporting Information is available free of charge on the ACS Publications website at DOI: 10.1021/acs.langmuir.9b01757.

> TEM image of cube-like ZrO2 CNCs; TEM images of cube-like ZrO2 CNCs prepared at different hydrothermal temperatures; XRD patterns of cube-like and star-like ZrO2 CNCs and ZrO2 nanocrystals; Zr 3d XPS spectra; FTIR spectra of cube-like and star-like ZrO2 CNCs, ZrO2 nanocrystals and ZrO2 CNCs coated with PVP; XRD patterns of cube-like and star-like ZrO2 CNCs and ZrO2 nanocrystals; Zr 3d XPS spectra of cube-like CNCs, star-like ZrO2 CNCs and ZrO2 nanocrystals; FTIR spectra of cube-like and star-like ZrO2 CNCs, ZrO2 nanocrystals and ZrO2 CNCs coated with PVP; degradation of RhB over the cube-like ZrO2 CNCs.; A): Ultraviolet-visible diffuse reflectance spectrum (UV-DRS) of the ZrO2 CNCs; and (B): Tauc plots $((\alpha h\nu)2$ vs. $h\nu))$ of the ZrO2 CNCs (the inset of both $(\alpha h\nu)1/2$ and $(\alpha h\nu)2$ vs. $h\nu$ in the absorption edge region); and Comparison of transient photocurrent response of star-like ZrO2 CNCs (a), P25 (b), cube-like ZrO2 CNCs (c), and aqueous dispersion of ZrO2 nanocrystals (d) (PDF)

■ AUTHOR INFORMATION

Corresponding Authors
*E-mail: sunqian@mail.buct.edu.cn (Q.S.).
*E-mail: wangjx@mail.buct.edu.cn (J.-X.W.).

ORCID ⊙
Dan Wang: 0000-0002-3515-4590
Xiao-Fei Zeng: 0000-0001-9010-0088
Jie-Xin Wang: 0000-0003-0459-1621

Notes
The authors declare no competing financial interest.

■ ACKNOWLEDGMENTS

■ REFERENCES

(1) Cargnello, M.; Doan-Nguyen, V. V. T.; Murray, C. B. Engineering Uniform Nanocrystals: Mechanism of Formation and Self-Assembly into Bimetallic Nanocrystal Superlattices. *AIChE J.* **2016**, *62*, 392−398.

(2) Wang, X.; Li, Y. Monodisperse Nanocrystals: General Synthesis, Assembly, and Their Applications. *Chem. Commun.* **2007**, *28*, 2901−2910.

(3) Chen, B.; Wang, J.-X.; Wang, D.; Zeng, X.-F.; Clarke, S. M.; Chen, J.-F. Synthesis of Transparent Dispersions of Aluminium Hydroxide Nanoparticles. *Nanotechnology* **2018**, *29*, 305605.

(4) Wang, J.-X.; Sun, Q.; Chen, B.; Wu, X.; Zeng, X.-F.; Zhang, C.; Zou, H.-K.; Chen, J.-F. Transparent "solution" of ultrathin magnesium hydroxide nanocrystals for flexible and transparent nanocomposite films. *Nanotechnology* **2015**, *26*, 195602.

(5) Lu, Z.; Yin, Y. Colloidal Nanoparticle Clusters: Functional Materials by Design. *Chem. Soc. Rev.* **2012**, *41*, 6874−6887.

(6) Yang, P.; Yuan, X.; Hu, H.; Liu, Y.; Zheng, H.; Yang, D.; Chen, L.; Cao, M.; Xu, Y.; Min, Y.; Li, Y.; Zhang, Q. Solvothermal Synthesis of Alloyed PtNi Colloidal Nanocrystal Clusters (CNCs) with Enhanced Catalytic Activity for Methanol Oxidation. *Adv. Funct. Mater.* **2018**, *28*, 1704774.

(7) Li, C.; Zhao, Y.; Li, F.; Shi, Z.; Feng, S. Near-Infrared Absorption of Monodisperse Water-Soluble PbS Colloidal Nanocrystal Clusters. *Chem. Mater.* **2010**, *22*, 1901−1907.

(8) Liu, J.; Sun, Z.; Deng, Y.; Zou, Y.; Li, C.; Guo, X.; Xiong, L.; Gao, Y.; Li, F.; Zhao, D. Highly Water-Dispersible Biocompatible Magnetite Particles with Low Cytotoxicity Stabilized by Citrate Groups. *Angew. Chem., Int. Ed.* **2010**, *48*, 5875−5879.

(9) Cao, S.-W.; Zhu, Y. J. Monodisperse α-Fe$_2$O$_3$ Mesoporous Microspheres: One-Step NaCl-Assisted Microwave-Solvothermal Preparation, Size Control and Photocatalytic Property. *Nanoscale Res. Lett.* **2011**, *6*, 1.

(10) Zhu, Y.; Zhao, W.; Chen, H.; Shi, J. A Simple One-Pot Self-Assembly Route to Nanoporous and Monodispersed Fe$_3$O$_4$ Particles with Oriented Attachment Structure and Magnetic Property. *J. Phys. Chem. C* **2007**, *111*, 5281−5285.

(11) Zellmer, S.; Garnweitner, G.; Breinlinger, T.; Kraft, T.; Schilde, C. Hierarchical Structure Formation of Nanoparticulate Spray-Dried Composite Aggregates. *ACS Nano* **2015**, *9*, 10749.

(12) Stolarczyk, J. K.; Deak, A.; Brougham, D. F. Nanoparticle Assemblies: Nanoparticle Clusters: Assembly and Control Over Internal Order, Current Capabilities, and Future Potential (Adv. Mater. 27/2016). *Adv. Mater.* **2016**, *28*, 5764.

(13) Lu, Z.; Gao, C.; Zhang, Q.; Chi, M.; Howe, J. Y.; Yin, Y. Direct Assembly of Hydrophobic Nanoparticles to Multifunctional Structures. *Nano Lett.* **2011**, *11*, 3404−3412.

(14) Hu, X.; Gong, J.; Zhang, L.; Yu, J. C. Continuous Size Tuning of Monodisperse ZnO Colloidal Nanocrystal Clusters by a Microwave-Polyol Process and Their Application for Humidity Sensing. *Adv. Mater.* **2008**, *20*, 4845−4850.

(15) Bai, F.; Wang, D.; Huo, Z.; Chen, W.; Liu, L.; Liang, X.; Chen, C.; Wang, X.; Peng, Q.; Li, Y. A Versatile Bottom-Up Assembly Approach to Colloidal Spheres from Nanocrystals. *Angew. Chem., Int. Ed.* **2007**, *46*, 6650−6653.

(16) Peng, B.; Zhang, X.; Aarts, D. G. A. L.; Dullens, R. P. A. Superparamagnetic Nickel Colloidal Nanocrystal Clusters with Antibacterial Activity and Bacteria Binding Ability. *Nat. Nanotechnol.* **2018**, *13*, 478−482.

(17) Xia, Y.; Nguyen, T. D.; Yang, M.; Lee, B.; Santos, A.; Podsiadlo, P.; Tang, Z.; Glotzer, S. C.; Kotov, N. A. Self-Assembly of Self-Limiting Monodisperse Supraparticles from Polydisperse Nanoparticles. *Nat. Nanotechnol.* **2012**, *7*, 580−587.

(18) Zhuang, J.; Dai, W.; Tian, Q.; Li, Z.; Xie, L.; Wang, J.; Liu, P.; Shi, X.; Wang, D. Photocatalytic Degradation of RhB over TiO$_2$

Bilayer Films: Effect of Defects and Their Location. *Langmuir* **2010**, *26*, 9686−9694.

(19) Kasinathan, K.; Kennedy, J.; Elayaperumal, M.; Henini, M.; Malik, M. Photodegradation of Organic Pollutants RhB Dye Using UV Simulated Sunlight on Ceria Based TiO₂ Nanomaterials for Antibacterial Applications. *Sci. Rep.* **2016**, *6*, 38064.

(20) Zhang, H.; Lv, X.; Li, Y.; Wang, Y.; Li, J. P25-Graphene Composite as a High Performance Photocatalyst. *ACS Nano* **2010**, *4*, 380−386.

(21) Sudrajat, H.; Babel, S. Comparison and Mechanism of Photocatalytic Activities of N-ZnO and N-ZrO₂ for the Degradation of Rhodamine 6G. *Environ. Sci. Pollut. Res.* **2016**, *23*, 10177−10188.

(22) Yu, W.; Zhang, J.; Peng, T. New Insight into the Enhanced Photocatalytic Activity of N-, C- and S-Doped ZnO Photocatalysts. *Appl. Catal., B* **2016**, *181*, 220−227.

(23) Faisal, M.; Ibrahim, A. A.; Harraz, F. A.; Bouzid, H.; Al-Assiri, M. S.; Ismail, A. A. SnO₂ Doped ZnO Nanostructures for Highly Efficient Photocatalyst. *J. Mol. Catal. A: Chem.* **2015**, *397*, 19−25.

(24) Wang, F.; Li, M.; Yu, L.; Fan, S.; Wang, Z.; Zhang, L.; Hao, Z.; Xu, X. Corn-Like, Recoverable γ-Fe₂O₃@SiO₂@TiO₂ Photocatalyst Induced by Magnetic Dipole Interactions. *Sci. Rep.* **2017**, *7*, 6960.

(25) Cui, Y.; Briscoe, J.; Wang, Y.; Tarakina, N. V.; Dunn, S. Enhanced Photocatalytic Activity of Heterostructured Ferroelectric BaTiO₃/α-Fe₂O₃ and the Significance of Interface Morphology Control. *ACS Appl. Mater. Interfaces* **2017**, *9*, 24518−24526.

(26) Jiao, Y.; Liu, Y.; Zhang, S.; Yin, B.; Qu, F.; Wu, X. Visible Light Driven α-Fe₂O₃ Nanorod Photocatalyst. *J. Nanosci. Nanotechnol.* **2014**, *14*, 7224−7227.

(27) Tian, H.; Teng, F.; Xu, J.; Lou, S.; Li, N.; Zhao, Y.; Chen, M. J. S. R. An Innovative Anion Regulation Strategy for Energy Bands of Semiconductors: A Case from Bi₂O₃ to Bi₂O(OH)₂SO₄. *Sci. Rep.* **2015**, *5*, 7770.

(28) Hezam, A.; Namratha, K.; Drmosh, Q. A.; Yamani, Z. H.; Byrappa, K. Synthesis of Heterostructured Bi₂O₃-CeO₂-ZnO Photocatalyst with Enhanced Sunlight Photocatalytic Activity. *Ceram. Int.* **2017**, *43*, 5292−5301.

(29) Shu, Z.; Jiao, X.; Chen, D. Hydrothermal Synthesis and Selective Photocatalytic Properties of Tetragonal Star-Like ZrO₂ Nanostructures. *CrystEngComm* **2013**, *15*, 4288−4294.

(30) Shu, Z.; Jiao, X.; Chen, D. Synthesis and Photocatalytic Properties of Flower-Like Zirconia Nanostructures. *CrystEngComm* **2012**, *14*, 1122−1127.

(31) Gionco, C.; Hernández, S.; Castellino, M.; Gadhi, T. A.; Muñoz-Tabares, J. A.; Cerrato, E.; Tagliaferro, A.; Russo, N.; Paganini, M. C. Synthesis and Characterization of Ce and Er Doped ZrO₂ Nanoparticles as Solar Light Driven Photocatalysts. *J. Alloys Compd.* **2019**, *775*, 896−904.

(32) Biswas, M.; Dinda, E.; Paira, T. K.; Roy, M.; Mandal, T. Gelation of Amino Acid-Based Amphiphiles in Water-Based Mixed Solvent Systems: Reusable Catalytic Templates for Nanostructured Silica and Silica-Zirconia Photocatalyst. *Soft Matter* **2013**, *9*, 5293−5304.

(33) Sadollahkhani, A.; Ibupoto, Z. H.; Elhag, S.; Nur, O.; Willander, M. Photocatalytic Properties of Different Morphologies of CuO for the Degradation of Congo red Organic Dye. *Ceram. Int.* **2014**, *40*, 11311−11317.

(34) Wang, W.; Wang, J.; Wang, Z. Z.; Wei, X. Z.; Liu, L.; Ren, Q. S.; Gao, W. L.; Liang, Y. J.; Shi, H. L. P-N Junction CuO/BiVO₄ Heterogeneous Nanostructures: Synthesis and Highly Efficient Visible-Light Photocatalytic Performance. *Dalton Trans.* **2014**, *43*, 6735−6743.

(35) Arshad, A.; Iqbal, J.; Mansoor, Q. NiO-Nanoflakes Grafted Graphene: An Excellent Photocatalyst and a Novel Nanomaterial for Achieving Complete Pathogen Control. *Nanoscale* **2017**, *9*, 16321−16328.

(36) Mateo, D.; Albero, J.; García, H. Graphene Supported NiO/Ni Nanoparticles as Efficient Photocatalyst for Gas Phase CO₂ Reduction with Hydrogen. *Appl. Catal., B* **2017**, *224*, 563−571.

(37) Zhang, N.; Liu, S.; Fu, X.; Xu, Y. J. A Simple Strategy for Fabrication of "Plum-Pudding" Type Pd@CeO₂ Semiconductor Nanocomposite as a Visible-Light-Driven Photocatalyst for Selective Oxidation. *J. Phys. Chem. C* **2011**, *115*, 22901−22909.

(38) Liyanage, A. D.; Perera, S. D.; Tan, K.; Chabal, Y.; Balkus, J. K. J. Synthesis, Characterization, and Photocatalytic Activity of Y-Doped CeO₂ Nanorods. *ACS Catal.* **2014**, *4*, 577−584.

(39) Feng, Z.; Zhang, M.; Ren, Q.; Mo, S.; Peng, R.; Yan, D.; Fu, M.; Chen, L.; Wu, J.; Ye, D. Design of 3-Dimensionally Self-Assembled CeO₂ Hierarchical Nanosphere as High Efficiency Catalysts for Toluene Oxidation. *Chem. Eng. J.* **2019**, *369*, 18−25.

(40) Xu, H.; Zhang, L. Controllable One-Pot Synthesis and Enhanced Photocatalytic Activity of Mixed-Phase TiO₂ Nanocrystals with Tunable Brookite/Rutile Ratios. *J. Phys. Chem. C* **2009**, *113*, 1785−1790.

(41) Tan, P.; Xi, C.; Wu, L.; Yan, Y. S.; Liu, W.; Pan, J.; Xiang, X. Hierarchical Flower-Like SnSe₂ Supported Ag₃PO₄ Nanoparticles: Towards Visible Light Driven Photocatalyst with Enhanced Performance. *Appl. Catal., B* **2017**, *202*, 326−334.

(42) Sinhamahapatra, A.; Jeon, J. P.; Kang, J.; Han, B.; Yu, J. S. Oxygen-Deficient Zirconia (ZrO₂₋ₓ): A New Material for Solar Light Absorption. *Sci. Rep.* **2016**, *6*, 27218.

(43) Neto, P. d. L.; Atik, M.; Avaca, L. A.; Aegerter, M. A. Sol-Gel ZrO₂ Coating for Chemical Protection of Stainless Steel. *J. Sol-Gel Sci. Technol.* **1994**, *1*, 177−184.

(44) Xia, Y.; Zhang, C.; Wang, J. X.; Wang, D.; Zeng, X. F.; Chen, J. F. Synthesis of Transparent Aqueous ZrO₂ Nanodispersion with a Controllable Crystalline Phase without Modification for a High-Refractive-Index Nanocomposite Film. *Langmuir* **2018**, *34*, 6806−6813.

(45) Xu, X.; Wang, X. Fine Tuning of the Sizes and Phases of ZrO₂ Nanocrystals. *Nano Res.* **2009**, *2*, 891−902.

(46) Li, W.; Huang, H.; Li, H.; Zhang, W.; Liu, H. Facile Synthesis of Pure Monoclinic and Tetragonal Zirconia Nanoparticles and Their Phase Effects on the Behavior of Supported Molybdena Catalysts for Methanol-Selective Oxidation. *Langmuir* **2008**, *24*, 8358−8366.

(47) Zhao, N.; Pan, D.; Nie, W.; Ji, X. Two-Phase Synthesis of Shape-Controlled Colloidal Zirconia Nanocrystals and Their Characterization. *J. Am. Chem. Soc.* **2006**, *128*, 10118.

(48) Luo, K.; Zhou, S.; Wu, L.; Gu, G. Dispersion and Functionalization of Nonaqueous Synthesized Zirconia Nanocrystals via Attachment of Silane Coupling Agents. *Langmuir* **2008**, *24*, 11497−11505.

(49) Garnweitner, G.; Goldenberg, L. M.; Sakhno, O. V.; Antonietti, M.; Niederberger, M.; Stumpe, J. Large-Scale Synthesis of Organophilic Zirconia Nanoparticles and their Application in Organic-Inorganic Nanocomposites for Efficient Volume Holography. *Small* **2007**, *3*, 1626−1632.

(50) Wessels, T.; Baerlocher, C.; Mccusker, L. B. Single-Crystal-Like Diffraction Data from Polycrystalline Materials. *Science* **1999**, *284*, 477.

(51) Baerlocher, C.; Mccusker, L. B.; Prokic, S.; Wessels, T. Exploiting Texture to Estimate the Relative Intensities of Overlapping Reflections. *Z. Kristallogr.* **2004**, *219*, 803−812.

(52) Grässlin, J.; Mccusker, L. B.; Baerlocher, C.; Gozzo, F.; Schmitt, B.; Lutterotti, L. Advances in Exploiting Preferred Orientation in the Structure Analysis of Polycrystalline Materials. *J. Appl. Crystallogr.* **2013**, *46*, 173−180.

(53) Deng, H.; Li, X.; Peng, Q.; Wang, X.; Chen, J.; Li, Y. Monodisperse Magnetic Single-Crystal Ferrite Microspheres. *Angew. Chem., Int. Ed.* **2005**, *44*, 2782−2785.

(54) Poyraz, A. S.; Kuo, C. H.; Biswas, S.; King'Ondu, C. K.; Suib, S. L. A General Approach to Crystalline and Monomodal Pore Size Mesoporous Materials. *Nat. Commun.* **2013**, *4*, 2952.

(55) Tsai, C.-L.; Liou, G. S. Highly Transparent and Flexible Polyimide/ZrO₂ Nanocomposite Optical Films with a Tunable Refractive Index and Abbe Number. *Chem. Commun.* **2015**, *51*, 13523−13526.

(56) Huang, H.; He, Y.; Lin, Z.; Kang, L.; Zhang, Y. Two Novel Bi-Based Borate Photocatalysts: Crystal Structure, Electronic Structure, Photoelectrochemical Properties, and Photocatalytic Activity under Simulated Solar Light Irradiation. *J. Phys. Chem. C* **2013**, *117*, 22986–22994.